

Article

Comprehensive Dynamic Interaction Studies in Inverter-Penetrated Power Systems

Fujian Li ^{*,†}  and Jin Ma [†] 

School of Electrical and Computer Engineering, The University of Sydney, Sydney 2006, Australia; j.ma@sydney.edu.au

* Correspondence: fujian.li@sydney.edu.au

† These authors contributed equally to this work.

Abstract: In a renewable-energy-penetrated power system (RPPS), inverter-based resources (IBRs) pose serious challenges to power system stability due to their completely different dynamic characteristics compared with conventional generators; thus, it is necessary to study the dynamic interactions between IBRs and power systems. Although many research efforts have been dedicated to this topic from both power electronics and power system researchers, some research from the power electronics field treats the external power system as a voltage source with an impedance, therefore ignoring the dynamic characteristics of a power system, while most of the research from the power system field applies simulation-based methods, for which it is difficult to directly interpret the interaction mechanism of IBRs and external system dynamics. Thus, none of these studies can explore the accurate dynamic interaction mechanism between IBRs and power systems, leading to performance degradation of IBR-integrated power systems. Our study takes into account the dynamic characteristics of both IBRs and the external power system, resulting in the development of a new open-loop transfer function for RPPSs. Based on this formulation, it is observed that under certain operating conditions, the dynamic interactions between the inverter and the power system help enhance IBR-penetrated power system stability compared with the case for which the external power system is controlled as a voltage source. The study also reveals how the inverter (phase-locked loop, control parameters, etc.), external power system (network strength) and penetration ratio in an IBR-penetrated power system affect the dynamic interactions between IBRs and the external power system using the proposed quantified interaction indices.



Citation: Li, F.; Ma, J. Comprehensive Dynamic Interaction Studies in Inverter-Penetrated Power Systems.

Energies **2024**, *17*, 2235. <https://doi.org/10.3390/en17092235>

Academic Editor: K. T. Chau

Received: 11 April 2024

Revised: 1 May 2024

Accepted: 3 May 2024

Published: 6 May 2024



Copyright: © 2024 by the authors. Licensee MDPI, Basel, Switzerland. This article is an open access article distributed under the terms and conditions of the Creative Commons Attribution (CC BY) license (<https://creativecommons.org/licenses/by/4.0/>).

Keywords: dynamic interaction; stability; inverter-based resource (IBR); network strength; renewable-penetrated power system

1. Introduction

Out of concern about the quick depletion of fossil fuels and their negative environmental impacts, the past decade has witnessed a fast increase in renewable energy generations [1–3]. However, the integration of renewable energy into the existing power grid poses new stability challenges due to the different dynamic characteristics of these IBRs from those of synchronous generators [4,5], which, in turn, often leads to curtailing renewable generation in order to maintain system stability [6], causing the waste of clean, renewable generating resources.

To address these challenges, one of the most urgent research topics for power system planners and operators is to explore and understand the dynamic interaction mechanisms between IBRs and power systems in order to help develop efficient methods to improve power system stability and better accommodate IBRs into existing systems. Meanwhile, a competent understanding of the interaction mechanisms also benefits power electronics engineers by providing them with more precise inverter design guidance, thus allowing them to take full advantage of inverter capability while maintaining the stability of the

power system. Although grid-forming inverter (GFMI) technology is currently a prominent research area due to its capability to support grid voltage and frequency, the majority of inverters deployed today function in grid-following inverter (GFLI) mode. Consequently, this paper explores the dynamic interactions between GFLI and the grid to better understand their operational mechanism.

Recent research on the interaction mechanism between IBRs and power systems can be divided into three categories:

- (1) In the field of power electronics, the external power grid is typically considered as an ideal voltage source with an impedance in renewable energy systems. This is referred to as a voltage source inverter system (VSIS), which takes into account various grid strengths and fully models renewable energy generators, particularly inverters. Based on this model, numerous studies have investigated the influences of inverter control on system stability as well as controller designs, with a focus on the impact analysis arising from phase angle tracking. The authors of [7] proposed a hybrid phase-locked loop (PLL) to improve the inverter's dynamic performance. The authors of [8] investigated the small-signal stability in low-inertia power systems and compared various control strategies through diverse bifurcation studies. The authors of [9–11] explored why a PLL deteriorates the stability of the inverter system, the extent of a PLL's influence, and how to improve the stability of a weak power system. While these researchers thoroughly account for the dynamic characteristics of PLLs, overlooking the dynamic characteristics of power systems prevents revealing the dynamic interactions between the IBRs and power systems.
- (2) In contrast to the aforementioned research, some stability studies on RPPSs adopt more detailed power system models, but they have simplified inverter models. The authors of [12–14] investigate how a high penetration of PVs affects a power system's static performance and transient stability. However, simplified inverter models are adopted in these studies. The authors of [15] developed a generic wind generator model for power system stability studies, but the inverter's PLL dynamics are neglected, which is, nevertheless, crucial to the stability of a weak power system. In this case, the incompleteness of the inverter model may lead to the final conclusions deviating from reality.
- (3) Among all the renewable-energy-penetrated power system dynamics studies, simulations are the most widely used approach. The major challenge of simulation-based approaches is that analysis and control are heavily related to pre-designed scenarios, making the research conclusions hard to generalize due to the inability to emulate all the possible operational scenarios [5,16]. Although simulations can analyze a system's dynamic characteristics at some operating points, a process of extensive and repeated simulations is required to study these characteristics across all crucial operating points. Furthermore, simulation-based approaches also face difficulties with revealing dynamic interaction mechanisms.

This paper employs a dq-impedance-based stability approach in the frequency domain to analyze the interaction dynamics and stability of RPPSs by considering the dynamics of both the IBR and the external power system. The model effectively captures their interactions by integrating the dynamics of both elements into a new transfer function matrix. Subsequently, multivariable control theory [17] is used to elucidate the dynamic interaction mechanisms between the IBR and the power system. In addition, the dynamic interactions are demonstrated through an RPPS under different factors, such as different PLLs, control parameters, SCRs and operating points. Furthermore, we also provide quantified indices to assess the impacts of interactions on stability, which, to our best knowledge, has not been done before. The major contributions of this paper are three-fold: (1) introduce a transfer function matrix for the first time that simultaneously contains dynamic information from both the inverter and the power system, (2) reveal the interaction mechanism of an IBR and an external power system through dq-impedance models with the influence of different factors, and (3) develop quantitative indices for the complex

interactions between an IBR and a power system. The research outputs of this work are of value not only to power system planners and operators, as the work sheds insights on the dynamic interaction mechanisms between IBRs and power systems, but also to power electronics engineers, as it provides useful guidance for inverter controller design with power system stability being considered.

The rest of the paper is structured as follows. Section 2 provides detailed modeling of the dynamic interactions of the RPPS and deduces the open-loop transfer function matrix. The dynamic interaction mechanism of the system is then explored using multivariable frequency domain control theory in Section 3. The consistency of dynamic interaction characteristics between theoretical analysis and simulation is then verified in Section 4. Section 5 concludes the whole paper.

2. Modeling Dynamic Interactions between an IBR and a Power System

For the sake of convenience, this paper analyzes a three-phase power system under the synchronous rotating reference frame (SRF), where the variables of the power system are described in the dq-vector form: $x_{abc} \rightarrow x_{dq} := (x_d, x_q)$, while the dq components of the inverter are under the inverter’s SRF. Therefore, the state and control variables of the IBR, SG, transmission line and load can be summarized in (1), (2) and (3), respectively. A coordinate transformation between the system reference and the inverter reference is required [18].

$$\begin{cases} \vec{x}_c = [i_{cdq}^s, v_{fdq}^s, P_{LPF}^s, V_{fLPF}^s, i_{cdq}^*, v_{cdq}^* \\ v_{dc}, i_{dc}^*, \omega_{PLL}, \theta_{PLL}] \\ \vec{u}_c = [P_{ref}, V_{fref}, v_{dcref}] \end{cases} \quad (1)$$

$$\begin{cases} \vec{x}_g = [E'_q, i_{gdq}, v_{gdq}, \omega_g, \delta] \\ \vec{u}_g = [P_{gref}, E_f, v_{gref}] \end{cases} \quad (2)$$

$$\begin{cases} \vec{x}_{cg} = [i_{ldq1}, i_{ldq}, i_{ldq2}, i_{fdq}, v_{fdq}, i_{gdq}, v_{gdq}] \\ \vec{u}_{cg} = [i_{fdq}, v_{fdq}, i_{gdq}, v_{gdq}] \end{cases} \quad (3)$$

Figure 1 shows an inverter-connected power system with a detailed control diagram of the GFLI. The transfer function model of the inverter has been widely studied in power electronics research papers and will be cited below while referring interested readers to [19–21]:

$$Y_c(s) = \frac{\Delta i_{cdq}}{\Delta v_{fdq}} = \begin{bmatrix} \frac{s^2 V_f + i_{cd}(sL_f/\omega_b + R_f)\omega_i\omega_p}{(sL_f/\omega_b + R_f)V_f(s^2 + \omega_i(s + \omega_p))} & \frac{i_{cq}(sG_{PLL}(s + \omega_i) + \omega_i\omega_p)}{V_f(s^2 + \omega_i(s + \omega_p))} \\ -\frac{I_{max}\omega_i\omega_v}{sV_f(s + \omega_i)} & \frac{sV_f - G_{PLL}(sV_f + i_{cd}(sL_f/\omega_b + R_f)(s + \omega_i))}{(sL_f/\omega_b + R_f)V_f(s + \omega_i)} \end{bmatrix} \quad (4)$$

where G_{PLL} is the transfer function of the PLL control loop; V_f is the amplitude of the inverter output voltage; I_{max} is the maximum output current of the inverter; and ω_p , ω_v and ω_i are the bandwidths of the active power loop, voltage loop and inner current loops, respectively.

Figure 2 shows the interaction model used in our work. The major modeling difference between other works and ours is demonstrated by comparing Figures 1 and 2. Other research works model the external power system as an ideal voltage source with series impedance, while herein we are going to establish a transfer function model of the external power system, including transmission lines, load and generator dynamics. Thus, in their models, v_{godq} and Z_g (i.e., Z_{gequ} in Figure 1) are real vectors/matrices, but in our models, they are all transfer functions of the complex frequency (s), with the closed-loop transfer function model of the whole system as:

$$\Delta i_{cdq} = (\Delta i_{codq} - Y_c(s) \cdot \Delta v_{godq}) \cdot \frac{1}{1 + Y_c(s) \cdot Z_g(s)}. \quad (5)$$

From (5), it can be seen clearly that $Y_c(s)Z_g(s)$ is the open-loop transfer function of the system and is a perfect candidate to explore the interaction mechanisms between IBR and the external power system, as $Y_c(s)$ represents the dynamics of the inverter, while $Z_g(s)$ is the dynamics of the external power system.

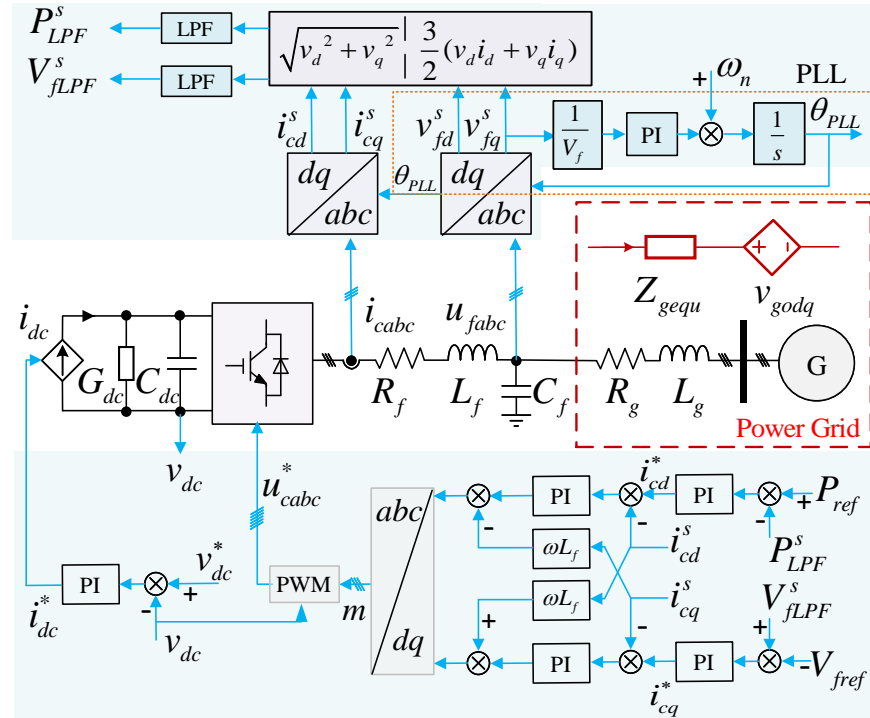


Figure 1. Control diagram of the grid-following inverter.

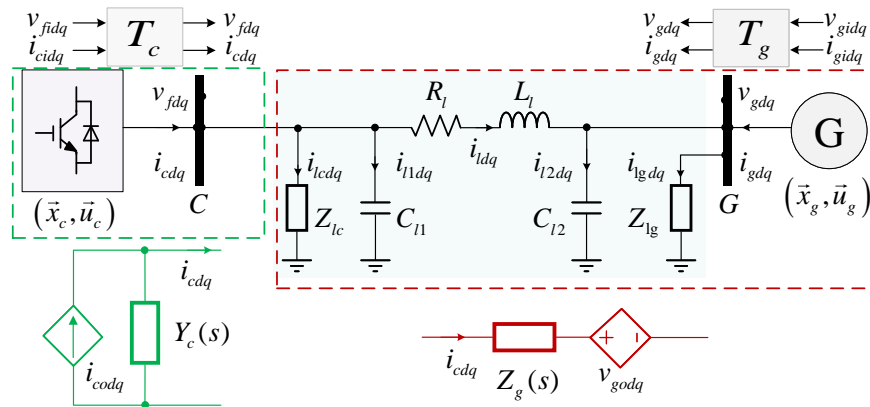


Figure 2. Schematic of the investigated 2-bus system.

2.1. Transfer Function on External Power System Dynamics

Without losing generality, the third-order SG model is adopted here as follows [22]. Undoubtedly, higher-order generator models can likewise be incorporated.

$$\begin{cases} \frac{d\delta}{dt} = \omega_b(\omega_g - 1) \\ \frac{d\omega_g}{dt} = \frac{1}{T_I}(P_m - P_e - D\omega_g) \\ \frac{T'd0}{x_d - x'd} \frac{dE'_q}{dt} = \frac{E_f}{x_d - x'd} - \frac{x_d E'_q}{x'd(x_d - x'd)} + \frac{U_g}{x'd} \cos \delta \end{cases} \quad (6)$$

where P_m and P_e are the mechanical and electromagnetic power, respectively, of the generator. The interface of SG and the network is modeled as follows:

$$\begin{cases} v_{gd} = -i_{gd}r - j i_{gq}x_q \\ v_{gq} = E'_q - i_{gq}r - j i_{gd}x'_d \end{cases} \quad (7)$$

Here, we apply a Laplace transform on Equations (6) and (7); then, combining the results through algebraic manipulation in the frequency domain yields:

$$\begin{bmatrix} \Delta v_{gd} \\ \Delta v_{gq} \end{bmatrix} = \begin{bmatrix} -r & x_q \\ G_{x'_d} & G_r \end{bmatrix} \begin{bmatrix} \Delta i_{gd} \\ \Delta i_{gq} \end{bmatrix} + \begin{bmatrix} 0 \\ G_{\Delta P_m} \end{bmatrix} \quad (8)$$

where the details of $G_{x'_d}$, G_r and $G_{\Delta P_m}$ are shown in Appendix A.

Furthermore, the transmission lines and loads can be modeled as (9). The nodal current balance constraint in the network is modeled as (10).

$$\begin{cases} \frac{dv_{fdq}}{dt} = \frac{\omega_b i_{1dq}}{C_{l1}} - j\omega_b \omega^* v_{fdq} \\ \frac{di_{1cdq}}{dt} = \frac{\omega_b v_{fdq}}{L_{zlc}} - \left(\frac{\omega_b R_{zlc}}{L_{zlc}} + j\omega_b \omega^* \right) i_{1cdq} \\ \frac{dv_{gdq}}{dt} = \frac{\omega_b i_{2dq}}{C_{l2}} - j\omega_b \omega^* v_{gdq} \\ \frac{di_{1gdq}}{dt} = \frac{\omega_b v_{gdq}}{L_{zlg}} - \left(\frac{\omega_b R_{zlg}}{L_{zlg}} + j\omega_b \omega^* \right) i_{1gdq} \\ \frac{di_{ldq}}{dt} = \frac{\omega_b (v_{fdq} - v_{gdq})}{L_l} - \left(\frac{\omega_b R_l}{L_l} + j\omega_b \omega^* \right) i_{ldq} \end{cases} \quad (9)$$

$$\begin{cases} i_{cdq} - i_{1cdq} - i_{1dq} - i_{ldq} = 0 \\ i_{gdq} - i_{1gdq} - i_{2dq} + i_{ldq} = 0 \end{cases} \quad (10)$$

Apply again the Laplace transform on Equations (9) and (10) and then eliminate the algebraic variables i_{1cdq} , i_{1dq} , i_{1gdq} and i_{2dq} . The transfer function matrix of the external power system dynamics, which takes into account the dynamics of generator and transmission lines as well as loads, can be succinctly formulated as follows:

$$\begin{bmatrix} \Delta v_{gdq} \\ \Delta i_{gdq} \end{bmatrix} = \begin{bmatrix} -\frac{Y_{cj}}{Y_{cjgk}} & \frac{1}{Y_{cjgk}} \\ \frac{Y_{cjgk}^2 - Y_{cj}Y_{gk}}{Y_{cjgk}} & \frac{Y_{gk}}{Y_{cjgk}} \end{bmatrix} \begin{bmatrix} \Delta v_{fdq} \\ \Delta i_{cdq} \end{bmatrix} \quad (11)$$

where Δv_{gdq} , Δi_{gdq} , Δv_{fdq} and Δi_{cdq} are complex variables; the expressions of Y_{cj} , Y_{gk} and Y_{cjgk} can be found in Appendix A.

2.2. Modeling Dynamic Interactions

Following the arguments below Equation (5), the equivalent impedance of the power system $Z_g(s)$ needs to be solved in order to use $Y_c(s)Z_g(s)$ for modeling the interactions between the IBR and the external dynamic system. For ease of understanding, pure resistive loads are utilized in this study. Nevertheless, it is noteworthy that the methods are also applicable to any other load models. Combining (8) with (11) gives:

$$\begin{bmatrix} \Delta v_{fd} \\ \Delta v_{fq} \end{bmatrix} = (\mathbf{B}_{j1} - \mathbf{X}_j \mathbf{Y}_j)^{-1} (\mathbf{X}_j \mathbf{B}_{j2} - \mathbf{Z}_j) \begin{bmatrix} \Delta i_{cd} \\ \Delta i_{cq} \end{bmatrix} + (\mathbf{B}_{j1} - \mathbf{X}_j \mathbf{Y}_j)^{-1} \begin{bmatrix} 0 \\ G_{\Delta P_m} \end{bmatrix} \quad (12)$$

where the details about \mathbf{Z}_j , \mathbf{X}_j , \mathbf{Y}_j , \mathbf{B}_{j1} and \mathbf{B}_{j2} can be examined in Appendix A.

Then, the impedance of the external power system can be expressed as:

$$\mathbf{Z}_g(s) = (\mathbf{B}_{j1} - \mathbf{X}_j \mathbf{Y}_j)^{-1} (\mathbf{X}_j \mathbf{B}_{j2} - \mathbf{Z}_j) \quad (13)$$

It should be noted that $Z_g(s)$ in (13) retreats into Z_{gs} of (14) when the dynamics of the external power system are neglected. Furthermore, the system's short-circuit ratio (SCR), which is widely used to assess the strength of a power system, is actually $SCR = \frac{1}{\|Z_{gs}\|}$ [19]. Therefore, both Z_{gs} and SCR are special cases of the general expression of $Z_g(s)$ proposed here.

$$Z_{gs} = \frac{1}{\frac{1}{R_{zlc}} + \frac{1}{\frac{1}{R_{zlg} + r + jx_d} + jL_1}} \quad (14)$$

From Equation (14), if the external power system is represented by a voltage source with internal impedance, the impedance can be simplified into a matrix form:

$$Z_{gequ} = \begin{bmatrix} sL_g/\omega_b + R_g & -L_g \\ L_g & sL_g/\omega_b + R_g \end{bmatrix} \quad (15)$$

where $R_g = \text{Re}[Z_{gs}]$ and $L_g = \text{Im}[Z_{gs}]$.

3. Dynamic Interactions Analysis

By applying the dynamic interaction model proposed in Section 2, this section analyzes the impact of various factors (SCR, PLL, control parameters and penetration ratio) on the stability of the entire system resulting from the dynamic interaction between the IBR and the external system. Case study parameters are shown in Table 1 [19].

Table 1. Parameters of the inverter.

Description	System Parameter	
	Symbol	Value
Output voltage amplitude, base value	U_{fb}	8163.97 V
Active power, base value	P_n	10 MW
Current, peak value	I_{max}	816.6 A
Filter inductance	L_f	0.33 p.u.
Filter resistance	R_f	0.00341 p.u.
Filter capacitance	C_f	0.015 p.u.
Bandwidth of the inner current loops	ω_i	1000 rad/s
Bandwidth of the voltage loop	ω_v	50 rad/s
Bandwidth of the active power loop	ω_p	10 rad/s
Natural angular frequency of the PLL	ω_{pll}	200 rad/s
Cut-off angular frequency of the LPFs	ω_{LPF}	200 rad/s

Since the transfer function models of the interaction have been established, Bode plots become a handy instrument to study how various control, network and operational factors influence the dynamic interactions between the IBR and the external power system. While the complicated interactions in the time domain can become much clearer when they are observed in the frequency domain, it is still challenging to quantify the interaction level. This issue becomes severe when considering a multi-input–multi-output (MIMO) dynamic system, as the proposed transfer function model matrix reflects the input/output characteristics of the entire system, while Bode plots can only reflect the channel-to-channel frequency characteristics.

To further quantify the interaction, the generalized Nyquist criterion (GNC) [21,23] is utilized by extending the classical Nyquist diagram into MIMO dynamic systems. It should be noted here that although GNC has been widely used in power electronics studies, it is rare to see its applications in power systems. Based on (4), (13) and (15), the generalized Nyquist diagram of the open-loop transfer function $Y_c Z_g$ and $Y_c Z_{gequ}$ is shown in Figure 3 for a weak power system with $SCR = 1$, where λ_1 and λ_2 are the eigenvalues of the respective transfer function matrix. The term (*margin*) can then be defined as $1 + L$, with L

being the value of the leftmost point in the generalized Nyquist diagram. The motivation to use this *margin* to reflect the dynamic interaction between the IBR and the system is two-fold: (1) it is a quantified value with clear and important physical meaning, as it measures the distance of the whole dynamic system towards being unstable; (2) it is an immediate consequence of the interactions between various IBR ($Y_c(s)$) and external system dynamics ($Z_g(s)$).

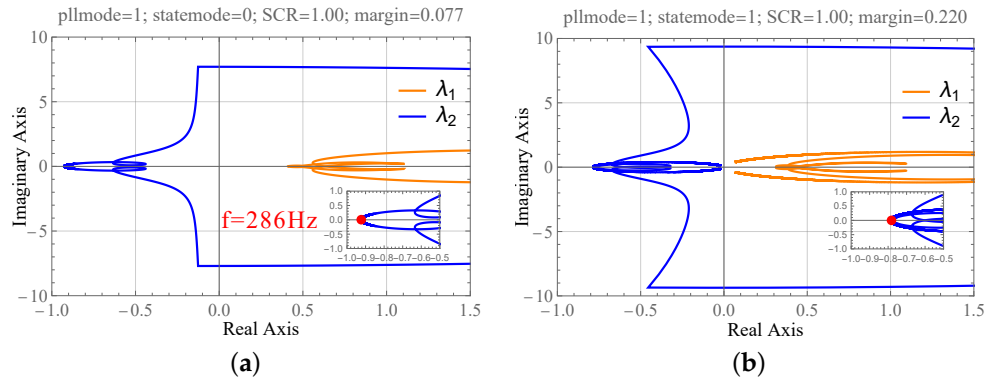


Figure 3. Nyquist plot of $Y_c Z_{gequ}$ and $Y_c Z_g$ with $SCR = 1$. (a) Nyquist plot of $Y_c Z_{gequ}$ and (b) Nyquist plot of $Y_c Z_g$.

This section will utilize the mentioned methods to analyze the dynamic interactions between the IBR and the external system. The analysis will be conducted under various factors such as grid strength, PLL, controller parameters and penetration ratio. To clearly and concisely describe system characteristics, henceforth we use $pllmode = 1$ and 2 to indicate the classical PLL controller design and the ideal PLL (which can always achieve phase tracking), respectively, and use $statemode = 1$ and 0 to indicate RPPS and VSIS, respectively.

3.1. SCR and Dynamic Interaction

3.1.1. RPPS with Different SCRs

SCR is a widely used grid strength index. Calculating SCR does not consider the system dynamics and is based on the grid impedance Z_{gequ} in (14). Typically, the power system is considered strong when $SCR \geq 3$ and weak when $SCR < 3$ [24]. The Bode plots of Z_{gequ} and Z_g at $SCR = 1$ (weak system) and 3 (strong system) are shown in Figure 4. Here, to reflect that both Y_c and Z_g are matrices, the following symbols are used: $Y_c = \{Y_c(DD), Y_c(DQ); Y_c(QD), Y_c(QQ)\}$, $Z_g = \{Z_g(DD), Z_g(DQ); Z_g(QD), Z_g(QQ)\}$ and $Y_c Z_g = \{Y_c Z_g(DD), Y_c Z_g(DQ); Y_c Z_g(QD), Y_c Z_g(QQ)\}$, where DD and QQ channels are decoupling channels, while DQ and QD channels are coupling channels.

Figure 4 shows that when the angular frequency $\omega > 2$ rad/s, the amplitudes of $Z_{g3(DD)}$ and $Z_{g3(QQ)}$ are smaller than those of $Z_{g1(DD)}$ and $Z_{g1(QQ)}$, respectively. This results in a reduction in the amplitudes of all channels of $Y_c Z_{g3}$, which can help to decrease the error in the control variable (Δi_{codq}) and output variable (Δi_{cdq}), as per Equation (5). Then, when $\omega < 15,000$ rad/s, the amplitudes of $Z_{g3(DQ)}$ and $Z_{g3(QD)}$ are smaller than those of $Z_{g1(DQ)}$ and $Z_{g1(QD)}$, respectively. This means that in a stronger power system, there is smaller dq-axis coupling, which is important for power electronics engineers for controller design as it reduces the requests for compensation in the dq-coupling in controller design and facilitates achieving the desired control objectives in each axis. Additionally, when systems with different SCRs have the same Y_c , the difference between $Y_c Z_{g1(DD)}$ ($Y_c Z_g(DD) = Y_c(DD) Z_g(DD) + Y_c(DQ) Z_g(QD)$) and $Y_c Z_{g3(DD)}$ mainly comes from the difference between $Z_{g1(DD)}$ and $Z_{g3(DD)}$ because the coupling terms have less effect. Specifically, at a frequency of approximately 1770 rad/s, the magnitude of $Y_c Z_{g3(QQ)}$ is much smaller than that of $Y_c Z_{g1(QQ)}$, and both of them are below 0 dB, indicating that $Y_c Z_{g3}$ has greater stability margins. This is in line with the results shown in Figure 5, which shows how the proposed interaction index changes with respect to changes in the grid strength.

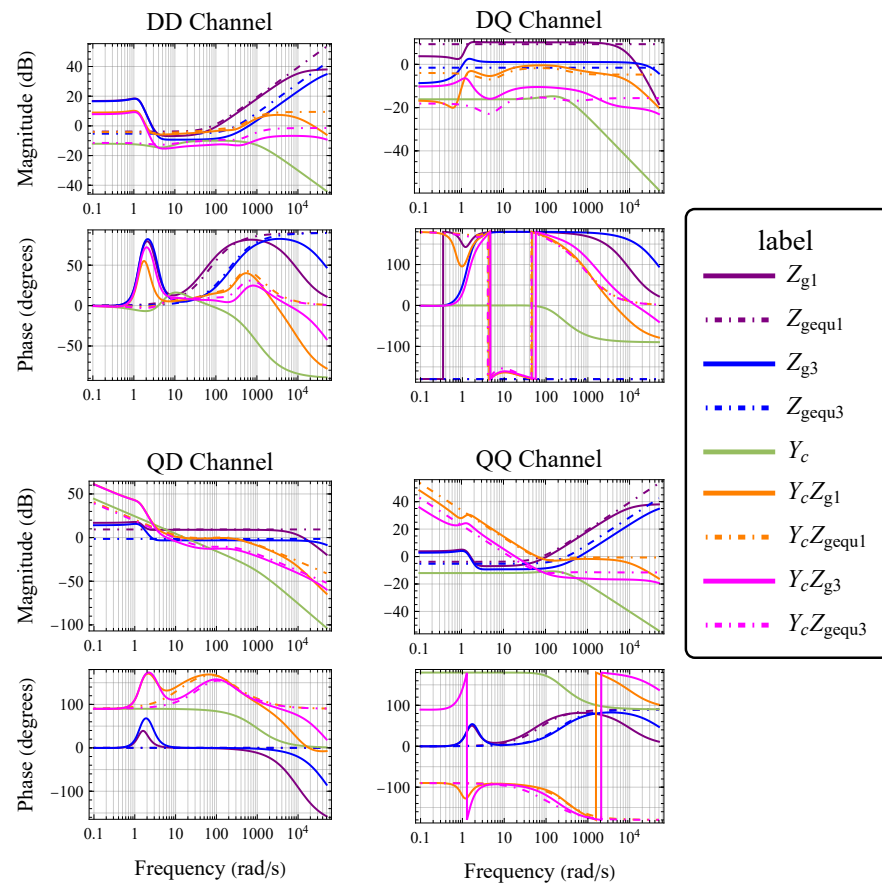


Figure 4. Bode plots of Z_g , Z_{gequ} , $Y_c Z_g$ and $Y_c Z_{gequ}$ with different SCRs. The numbers in the subscript represent the values of SCRs.

Therefore, a system with higher SCR has lower coupling between the d-axis and q-axis, lower control error and higher interaction index. On the other hand, for power electronics engineers, a power system with a higher SCR also means the controller is more easily designed and more robust.

3.1.2. RPPS vs. VSIS

As shown in Figure 4, in the middle-frequency range, under the same SCR, there is a noticeable similarity in the frequency responses of both Z_g and Z_{gequ} in all channels. However, over almost the entire frequency range, $Z_g(DD)$ and $Z_g(QQ)$ have a lower magnitude than $Z_{gequ}(DD)$ and $Z_{gequ}(QQ)$, respectively. This indicates that the system has a lower control error regarding any changes in the input if the system’s dynamic is considered compared with the VSIS model. In the high-frequency range, the magnitudes of all channels of Z_{gequ} are higher than those of Z_g , suggesting that the system is more prone to high-frequency oscillation in VSIS.

In the middle-frequency domain, Bode plots of $Y_c Z_g$ and $Y_c Z_{gequ}$ have similar shapes in all channels, which means the two systems have similar dynamics within this frequency range. Moreover, Figure 4 shows that, compared to $Y_c Z_{gequ}$, the magnitudes of all channels of $Y_c Z_g$ attenuate extremely fast at high frequencies, indicating that there is much lower possibility of high-frequency oscillations in RPPS. $Y_c Z_g(QQ)$ and $Y_c Z_{gequ}(QQ)$ have almost the same phase Bode plots when the external power systems have the same SCR. However, when $\omega = 1770$ rad/s (268 Hz), $Y_c Z_{gequ1}(QQ)$ has almost no stability margin, while $Y_c Z_{g1}(QQ)$ still has a stability margin. This indicates that RPPS is more stable than VSIS under these conditions as dynamic interactions between IBR and the power system are taken into account, which is consistent with Figure 3.

Figure 5 shows that the dynamic interaction index increases with increasing SCR. It can be seen clearly for a very weak power system that the interactions between IBR and the external system have discernible differences for different external system dynamics (RPPS and VSIS). The increasing SCR can help reduce the impact of external system dynamics on its interactions with IBR. It can also be observed that RPPS always lies above VSIS, indicating that the interactions between the external system dynamics and the IBR actually improve the system stability level. This can be attributed to the frequency spectrum dynamic performances introduced by the coherent inertia of the generators, as can be observed through the Bode plot studies in Figure 4.

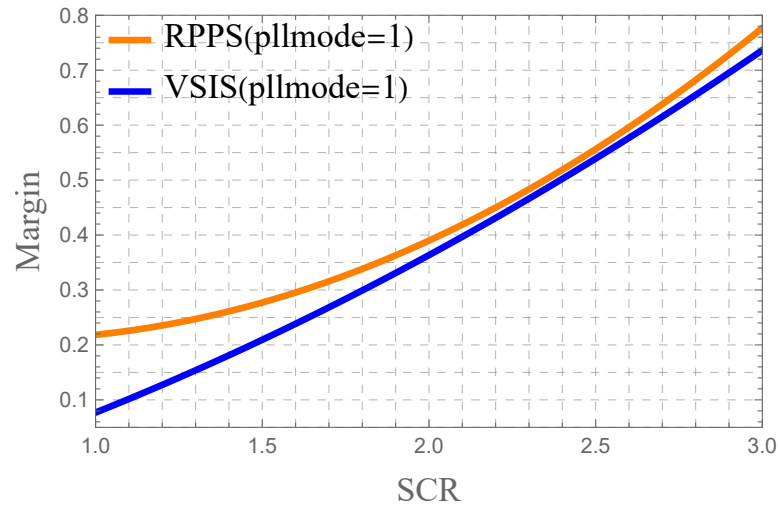


Figure 5. Margins of RPPS and VSIS with different SCRs. The margin value comes from the GNC of the system's open-loop transfer function.

3.2. PLL and Dynamic Interaction

3.2.1. RPPS with different PLLs

Figure 6 demonstrates how the PLL influences the characteristics of the IBR and then affects the interaction between IBRs and the external power system when $SCR = 1$. Y_{caf} (a new Y_c when the PLL of the IBR is ideal) still has the same characteristics as Y_c in DD and QD channels, but when $3 \text{ rad/s} < \omega < 2000 \text{ rad/s}$, the magnitude of $Y_{caf(DQ)}$ is smaller than that of $Y_{c(DQ)}$, which can reduce the coupling between the d-axis and q-axis of Y_{caf} . When $\omega < 300 \text{ rad/s}$, the magnitude of $Y_{caf(QQ)}$ is smaller than that of $Y_{c(QQ)}$, which is beneficial for Y_{caf} to improve system stability. When $\omega = 1770 \text{ rad/s}$ and the phase equals -180 degrees, the magnitude margin of $Y_c Z_{g(QQ)}$ is very small, which can potentially cause the system to become unstable. However, at a frequency of 300 rad/s and a phase angle of -180 degrees, $Y_{caf} Z_{g(QQ)}$ still has a significant magnitude margin.

Several researchers have examined the effects of PLLs on the system to improve PLL performance to increase system stability in weak power systems [7,9,10,19]. Different from such studies, this paper provides an intuitive demonstration of the PLL's impacts on the system dynamics using the proposed interaction index, which can provide guidance for power electronic engineers to enhance PLL design. Figure 7 shows how the proposed interaction index changes under the influence of the PLL and the change in I_{cq} , which represents different operating points. When $pllmode = 2$, the system has an improved interaction index, demonstrating that PLL has a negative impact on the interactions between IBR dynamics and the external power system.

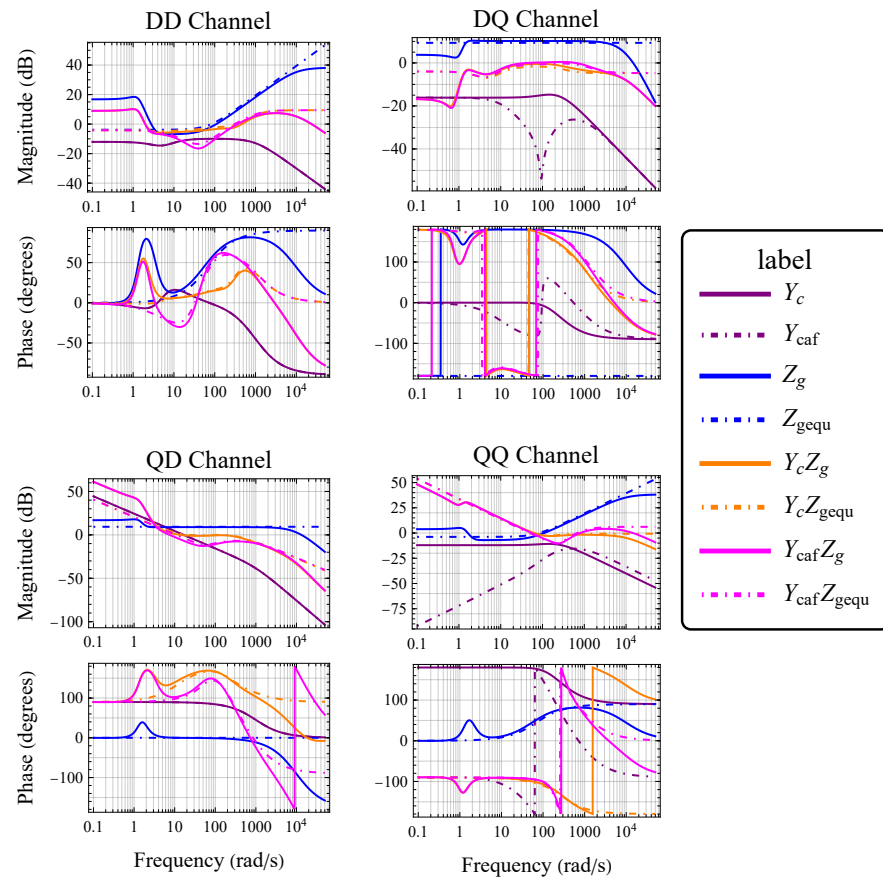


Figure 6. Bode plots of $Y_c, Y_{caf}, Y_cZ_g, Y_{caf}Z_g$ under the effect of PLL.

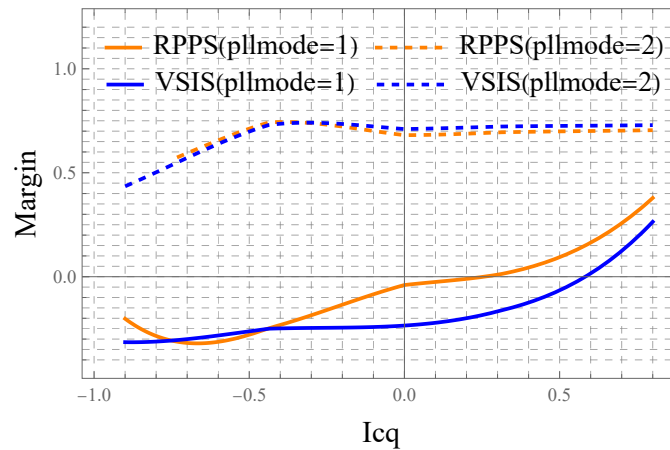


Figure 7. Stability margins of RPPS and VSIS under the effect of PLL. The variable I_{cq} represents the per-unit value of IBR, and different values of I_{cq} indicate that the system operates in different states.

3.2.2. RPPS vs. VSIS

Based on Figure 7, it is evident that the interaction indices of RPPS and VSIS remain similar across different operating points when utilizing an ideal PLL. For the system with a traditional PLL, the index of RPPS is above that of VSIS for most operation points, which demonstrates that the interactions between external system dynamics and IBR dynamics increase the whole system’s stability level, which is consistent with the observations from Figure 6. This also indicates that the dynamic interactions between the IBR and the external system hinge heavily on the interactions between the PLL and the external dynamics.

3.3. Control Parameters and Dynamic Interaction

Selecting the bandwidths for different control blocks in an IBR is critical in inverter controller design. Five bandwidths need to be decided in Figure 1: namely, ω_i , ω_v , ω_p , ω_{pll} and ω_{LPF} , corresponding to the bandwidths of inner current loop, voltage loop, active power control loop, PLL controller and the low-pass filter, respectively. Among them, ω_i and ω_{pll} have the most significant influence on the interaction. Based on Figure 8, varying combinations of ω_i and ω_{pll} result in different frequency responses for Y_c and thus different effects on $Y_c Z_g$. Specifically, (1) Y_{c1} and Y_{c4} , as well as Y_{c2} and Y_{c3} , have the same ω_i and exhibit the same frequency response in the DD and QD channels, indicating that ω_{pll} has no effect on these two channels; (2) Y_{c1} and Y_{c2} , as well as Y_{c3} and Y_{c4} , have the same ω_{pll} and the same frequency response in the DQ and QQ channels, suggesting that ω_i has little effect on these two channels; (3) optimal stability occurs at $\omega_i = 3000$ and $\omega_{pll} = 50$, where the phase angle equals -180 degrees and the amplitude margin of $Y_{c3} Z_g(QQ)$ is the largest, which is consistent with the peak point in Figure 9.

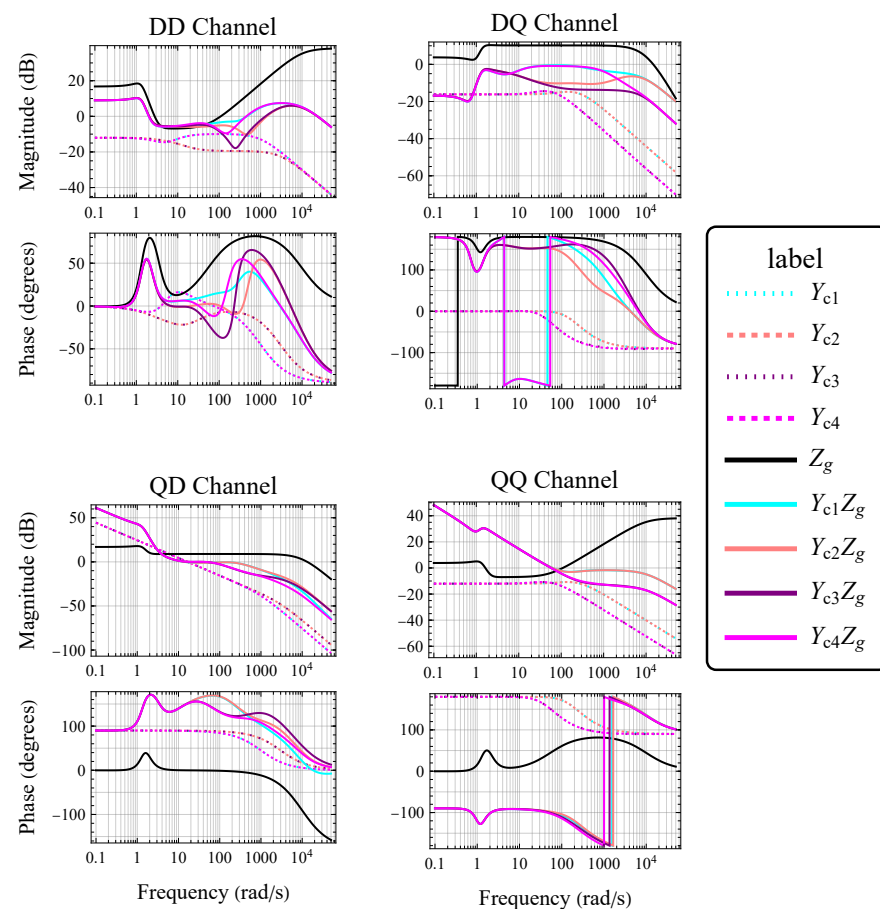


Figure 8. Bode plots of Y_c and $Y_c Z_g$ with different controller parameters (ω_i and ω_{pll}). The numbers in the subscript represent different combinations of control parameters: “1” means $\omega_i = 1000$ rad/s and $\omega_{pll} = 200$ rad/s, “2” means $\omega_i = 3000$ rad/s and $\omega_{pll} = 200$ rad/s, “3” means $\omega_i = 3000$ rad/s and $\omega_{pll} = 50$ rad/s, and “4” means $\omega_i = 1000$ rad/s and $\omega_{pll} = 50$ rad/s.

The proposed index can be used to evaluate the dynamic sensitivity of the system stability with respect to these key control parameters. Figure 9 illustrates how the index changes regarding the different combinations of ω_i and ω_{pll} . The figure of contours shows the region where the choice of ω_i and ω_{pll} can make the whole system unstable as well as how to tune the key parameters of the IBR to increase the whole system’s stability by leveraging the interaction between the IBR and the external system dynamics. Both, we believe, are very beneficial to power electronics engineers for IBR controller design.

Therefore, this paper can form a handy tool for inverter controller designers for finding reasonable parameters with system stability being considered. It should also be noted that from Figure 9b, in the region where $\omega_i > 1200$ rad/s and $\omega_{pll} > 50$ rad/s, the dynamic interaction between the IBR and the generator dynamics contributes to improvement in the stability level compared to that between the IBR and the static external system.

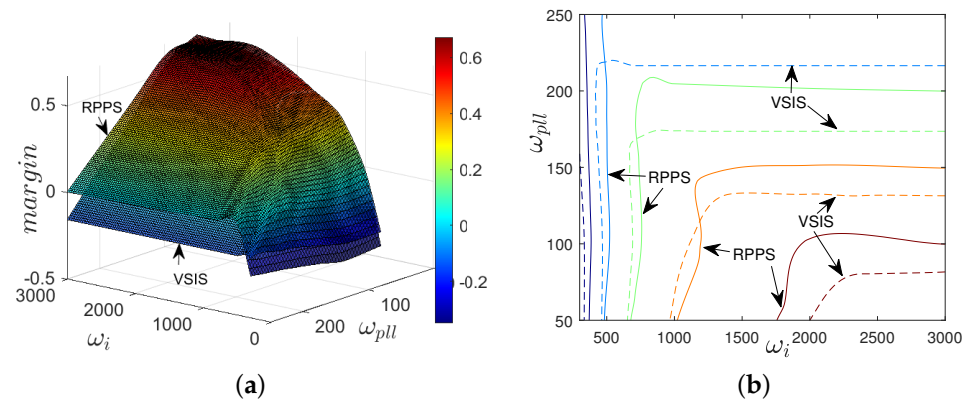


Figure 9. Impact of controller parameters (ω_i and ω_{pll}) on the stability of the system in RPPS and VSIS. In (b), the solid line represents RPPS and the dashed line represents VSIS. (a) Change in index with respect to current loop bandwidth and PLL bandwidth. (b) Contours of margin.

3.4. Penetration Ratio and Dynamic Interaction

The ratio between the IBR's real power output and the total generation in the whole system is widely used as a measure of the IBR's penetration level. As shown in Figure 10, when the penetration ratio equals 0.25 or 0.75 and the angular frequency $\omega > 100$, Y_{c1} and Y_{c2} , as well as Z_{g1} and Z_{g2} , have very similar frequency responses in DD, DQ and QD channels. However, the magnitude of $Y_{c1(QQ)}$ is smaller than that of $Y_{c2(QQ)}$, which leads to the magnitude of $Y_{c1}Z_{g1(QQ)}$ being much lower than 0 dB compared to $Y_{c2}Z_{g1(QQ)}$ when the phase angle equals -180 degrees. Therefore, a lower penetration ratio can result in better stability for the RPPS.

From Figure 11, it can be seen that the interaction index decreases with the increase in the penetration ratio regardless of the power system model adopted. As this interaction index aligns with the stability level of the whole system, the decreasing index with the increase in IBR penetration indicates that the GFLI reduces the stability level of the system, and its negative impacts increase along with the penetration level.

Furthermore, when using the VSIS model, the interaction index declines more quickly with respect to the increase in IBR penetration. Specifically, the critical value of the penetration ratio using the VSIS model is approximately 0.6, whereas, with the RPPS model, it is approximately 0.8, which means that the interactions between the IBR and VSIS have more severe adverse impacts on the stability of the system. This confirms the earlier observation that interaction between the IBR and generator dynamics might improve the system stability under certain operational scenarios as outlined in Section 3.1.2.

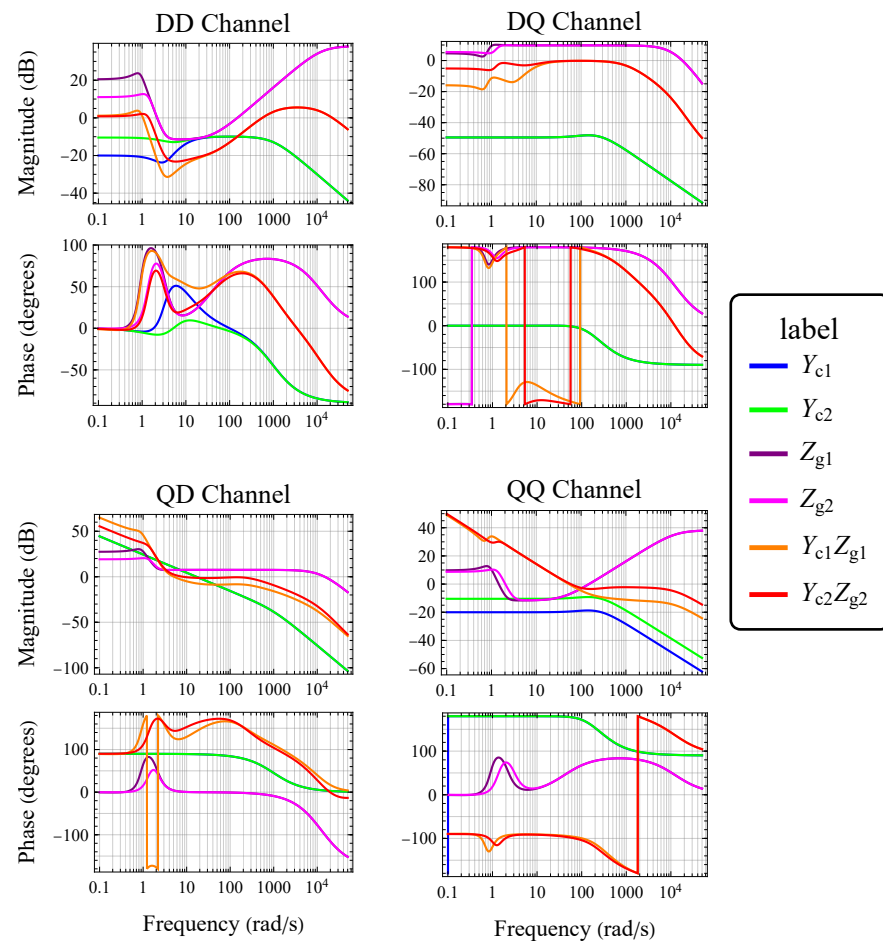


Figure 10. Bode plots of Y_{c1} , Y_{c2} , Z_{g1} , Z_{g2} , $Y_{c1}Z_{g1}$ and $Y_{c2}Z_{g2}$ with different IBR penetration levels. The subscript “1” means the penetration ratio equals 0.25, and the subscript “2” represents penetration ratios equal to 0.75.

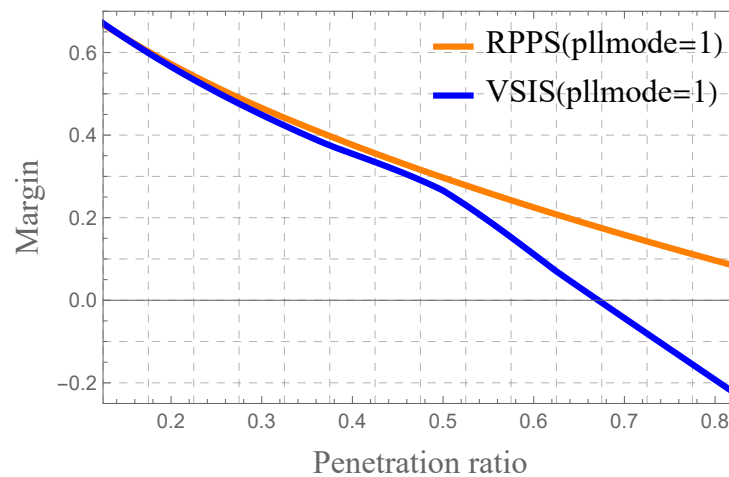


Figure 11. Dynamic interaction index with different IBR penetration levels.

4. Simulation Results

Numeric simulation studies are carried out to validate the developed IBR-integrated power system model and the correctness of the proposed index. Detailed Simulink models corresponding to the analytical models in Section 2 are developed. The steady-state values are shown in Table 2, and the controller parameters of the IBR are identical to those in Table 1.

Table 2. Design parameters of the simulation.

Description	System Parameter	
	Symbol	Value
D-axis component of inverter output current	i_{cd}	0.25 p.u.
Q-axis component of inverter output current	i_{cq}	0.156 p.u.
D-axis component of initial output voltage	v_{gd}	0.677 p.u.
Q-axis component of initial output voltage	v_{gq}	0.736 p.u.
D-axis component of initial output current	i_{gd}	0.75 p.u.
Q-axis component of initial output current	i_{gq}	0.66 p.u.
Load at the inverter side	R_{zlc}	60 p.u.
Load at the SG side	R_{zlg}	0.803 p.u.
Inductance of the transmission line	L_l	2.59 p.u.

Based on the system's designed parameters and the operation point, the interaction index of RPPS is 0.22, indicating that the system is stable. However, the interaction index of VSIS is around 0.077, which is at the edge of stability. The trajectories of IBR voltage and active and reactive power are shown in Figure 12 for two different dynamically interacting systems in the paper. The disturbance is created by adding a 3 MW load at the inverter terminal bus between 5 s and 5.1 s. The simulation results fully validate the theoretical analysis results: (i) the RPPS shown in Figure 12a remains stable after experiencing the numerical disturbances; (ii) the VSIS shown in Figure 12b, although still stable initially due to the positive interaction index, finally loses its stability because of the disturbance, which confirms it is at the edge of stability. Compared with the frequency domain analysis in the previous sections, it should be noted that the time domain simulation reveals whether a system is stable or unstable, but it cannot clearly provide the margin to instability and unveil how the IBR interacts with the external system dynamics to affect system stability.

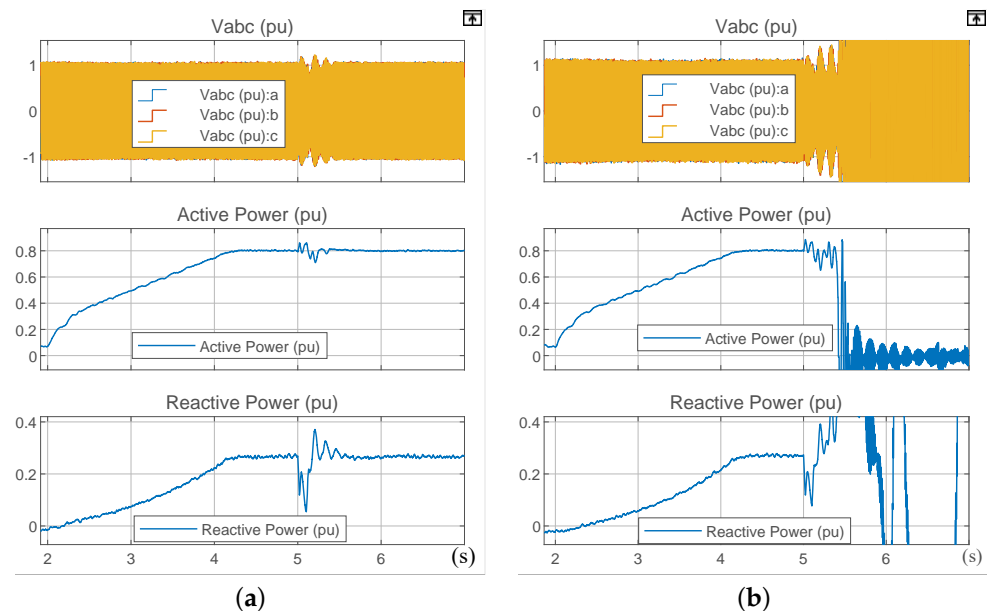


Figure 12. Voltage, active power and reactive power at C-bus of RPPS and VSIS. (a) RPPS ($SCR = 1$). (b) VSIS ($SCR = 1$).

As described in Section 3.1, the interaction index of RPPS is 0.22 when $SCR = 1$, whereas the interaction index is 0.76 when $SCR = 3$. This means the RPPS with $SCR = 3$ has a larger stability margin and very strong anti-interference capability owing to its larger interaction index compared to the RPPS with $SCR = 1$. To verify that systems with various SCRs have different interaction indices, we build two other simulations for which these two systems with different SCRs remain stable before 5 s and then suffer from a disturbance,

as shown in Figure 13. The disturbance is created by adding a 5 MW load at the terminal bus of the inverter between 5 s and 5.1 s. The simulation results show: (i) the RPPS with $SCR = 1$ shown in Figure 13a loses stability after the disturbance; (ii) the RPPS with $SCR = 3$ shown in Figure 12b remains stable after the disturbance, which is attributable to its higher positive interaction index.

Combining Figure 12 and Figure 13, it can be observed that the RPPS with $SCR = 1$ can withstand a 3 MW disturbance but loses stability under a 5 MW disturbance. However, the RPPS with $SCR = 3$ is capable of maintaining stability when suffering from the 5 MW disturbance, which is a result of its larger interaction index compared to that of $SCR = 1$. Therefore, the interaction index provides an intuitive way to reflect all factors that impact system interactions.

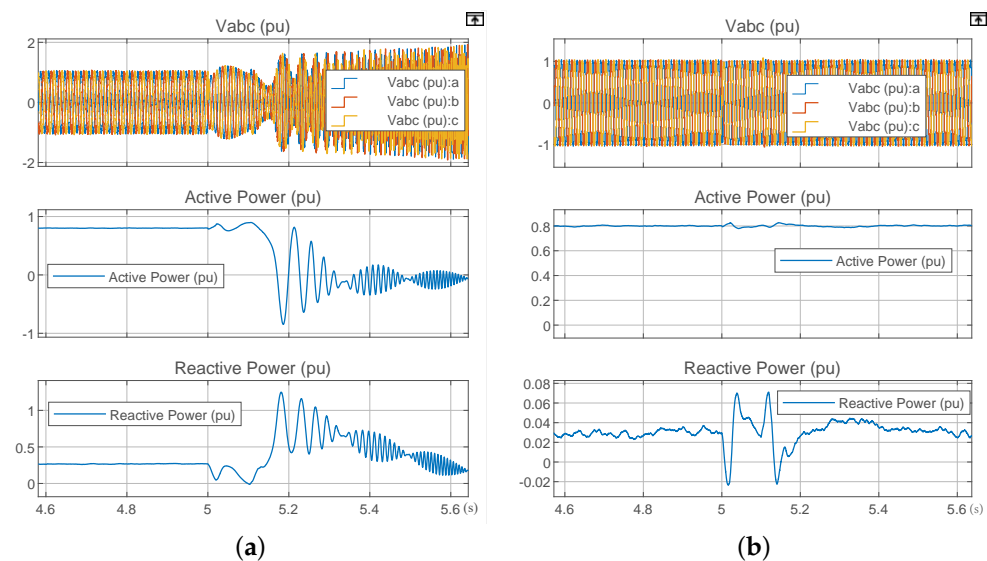


Figure 13. Voltage, active power and reactive power at C-bus of RPPS with different SCRs. (a) RPPS ($SCR = 1$). (b) RPPS ($SCR = 3$).

5. Conclusions

This paper derives a new transfer function matrix of a system by considering both the dynamic characteristics of the IBR and the external power system simultaneously for the first time. Not only can the respective dynamic characteristics of the IBR and the external system be revealed by analyzing the newly developed transfer function matrix from a frequency domain perspective, but we can also determine how they interact with each other. This paper proposes a numerical index to quantify the interaction impacts of inverter-based resources (IBRs) on overall system stability. Through a detailed examination of the dynamics between the IBR and two distinct external power system models, we find significant differences in stability outcomes, highlighting the critical need for in-depth studies of these interactions. Furthermore, the study conducts an extensive sensitivity analysis of the system's stability in relation to network strength, control components, controller parameters and penetration levels. These insights are invaluable for power system planners, operators and inverter design engineers and offer targeted guidance for enhancing system robustness. Extending research to a grid-forming inverter and a multi-machine power system is undergoing.

Author Contributions: Conceptualization, F.L. and J.M.; methodology, F.L. and J.M.; software, F.L.; validation, F.L. and J.M.; formal analysis, F.L.; writing—original draft preparation, F.L.; writing—review and editing, J.M.; supervision, J.M. All authors have read and agreed to the published version of the manuscript.

Funding: This research received no external funding.

Data Availability Statement: The data provided in the article are sufficient to reproduce the results.

Conflicts of Interest: The authors declare no conflicts of interest.

Abbreviations

The following abbreviations are used in this manuscript:

SG	Synchronous generator
RPPS	Renewable-penetrated power system
VSIS	Voltage source inverter system
PLL	Phase-locked loop
SRF	Synchronous rotating reference frame
SCR	Short-circuit ratio
GNC	Generalized Nyquist criterion
IBR	Inverter-based resource
i_{cdq}^*	Reference value of inverter output current
v_{cdq}^*	Reference value of inverter output voltage
ω_{PLL}	PI output value in the PLL
P_{ref}, V_{fref}	Reference values of inverter’s power and voltage
E_f	Excitation voltage of an SG
E'_q	Q-axis transient electromotive force of an SG
ω_g	Angular frequency of an SG
δ	Phase of rotor of an SG
i_{ldq}	Current on transmission line
v_{fdq}	Output capacitor voltage of inverter
i_{gdq}, v_{gdq}	Output current and output voltage of an SG
P_{gref}, v_{gref}	Reference values of SG’s output power and voltage
i_{cdq}, v_{cdq}	Output current and output voltage of an inverter
Δi_{codq}	Small signal for equivalent current source of inverter
Δv_{godq}	Small signal for equivalent voltage source of SG
D, T_J	Damping coefficient and inertia coefficient
T'_{d0}	D-axis transient time constant of SG

Appendix A

$$\begin{cases} G_{x'd} = \frac{-G_{Eq}v_{gd} + G_{Eq}r_{igd} - x'd}{G_{Eq}i_{gq} + 1} \\ G_r = \frac{-G_{Eq}v_{gq} - G_{Eq}x_q i_{gd} - r}{G_{Eq}i_{gq} + 1} \\ G_{\Delta P_m} = \frac{G_{Eq} \cdot \Delta P_m}{G_{Eq}i_{gq} + 1} \\ G_{Eq} = -\frac{(x_d - x'd)v_{gd}}{(sx'dT'_{d0} + x_d)s / \omega_b \cdot (sT_J + D)} \end{cases} \tag{A1}$$

$$\begin{cases} Y_{cj} = \frac{\omega_b}{sL_{zlc} + \omega_b R_{zlc} + j\omega_b \omega^* L_{zlc}} + \frac{(s + j\omega_b \omega^*)C_{l1}}{\omega_b} \\ \quad + \frac{\omega_b}{sL_l + \omega_b R_l + j\omega_b \omega^* L_l} \\ Y_{gk} = \frac{\omega_b}{sL_{zlg} + \omega_b R_{zlg} + j\omega_b \omega^* L_{zlg}} + \frac{(s + j\omega_b \omega^*)C_{l2}}{\omega_b} \\ \quad + \frac{\omega_b}{sL_l + \omega_b R_l + j\omega_b \omega^* L_l} \\ Y_{cjgk} = -\frac{\omega_b}{sL_l + \omega_b R_l + j\omega_b \omega^* L_l} \end{cases} \tag{A2}$$

$$\begin{cases} \mathbf{Z}_j = \begin{bmatrix} sL_l & -L_l\omega^* \\ L_l\omega^* & sL_l \end{bmatrix}; \mathbf{B}_{j1} = \begin{bmatrix} -\frac{sL_l}{R_{zlc}} - 1 & \frac{L_l\omega^*}{R_{zlc}} \\ -\frac{L_l\omega^*}{R_{zlc}} & -\frac{sL_l}{R_{zlc}} - 1 \end{bmatrix}; \\ \mathbf{X}_j = \begin{bmatrix} -r & x_q \\ G_{x'd} & G_r \end{bmatrix}; \mathbf{B}_{j2} = \begin{bmatrix} \frac{sL_l}{R_{zlg}} + 1 & -\frac{L_l\omega^*}{R_{zlg}} \\ \frac{L_l\omega^*}{R_{zlg}} & \frac{sL_l}{R_{zlg}} + 1 \end{bmatrix}; \\ \mathbf{Y}_j = \begin{bmatrix} -\frac{sL_l}{R_{zlc}R_{zlg}} - \frac{1}{R_{zlg}} - \frac{1}{R_{zlc}} & \frac{L_l\omega^*}{R_{zlc}R_{zlg}} \\ -\frac{L_l\omega^*}{R_{zlc}R_{zlg}} & -\frac{sL_l}{R_{zlc}R_{zlg}} - \frac{1}{R_{zlg}} - \frac{1}{R_{zlc}} \end{bmatrix}. \end{cases} \quad (\text{A3})$$

References

1. Taylor, J.A.; Dhople, S.V.; Callaway, D.S. Power Systems without Fuel. *Renew. Sustain. Energy Rev.* **2016**, *57*, 1322–1336. [\[CrossRef\]](#)
2. Tester, J.W.; Drake, E.M.; Driscoll, M.J.; Golay, M.W.; Peters, W.A. *Sustainable Energy, Second Edition: Choosing Among Options*; MIT Press: Cambridge, MA, USA, 2012.
3. Colak, I.; Kabalci, E.; Fulli, G.; Lazarou, S. A Survey on the Contributions of Power Electronics to Smart Grid Systems. *Renew. Sustain. Energy Rev.* **2015**, *47*, 562–579. [\[CrossRef\]](#)
4. Shafiullah, M.; Ahmed, S.D.; Al-Sulaiman, F.A. Grid Integration Challenges and Solution Strategies for Solar PV Systems: A Review. *IEEE Access* **2022**, *10*, 52233–52257. [\[CrossRef\]](#)
5. Sun, J.; Li, M.; Zhang, Z.; Xu, T.; He, J.; Wang, H.; Li, G. Renewable Energy Transmission by HVDC across the Continent: System Challenges and Opportunities. *CSEE J. Power Energy Syst.* **2017**, *3*, 353–364. [\[CrossRef\]](#)
6. Li, Y.; Wang, R.; Zhou, W.; Gao, B. Evaluation of Dispatching Results of Power System with High Penetration of Renewable Energy Based on Pythagorean Fuzzy Set and TOPSIS. *Energy Rep.* **2022**, *8*, 524–532. [\[CrossRef\]](#)
7. Hadjidemetriou, L.; Kyriakides, E.; Blaabjerg, F. A New Hybrid PLL for Interconnecting Renewable Energy Systems to the Grid. *IEEE Trans. Ind. Appl.* **2013**, *49*, 2709–2719. [\[CrossRef\]](#)
8. Markovic, U.; Vorwerk, J.; Aristidou, P.; Hug, G. Stability Analysis of Converter Control Modes in Low-Inertia Power Systems. In Proceedings of the 2018 IEEE PES Innovative Smart Grid Technologies Conference Europe (ISGT-Europe), Sarajevo, Bosnia and Herzegovina, 21–25 October 2018; pp. 1–6. [\[CrossRef\]](#)
9. Wen, B.; Boroyevich, D.; Burgos, R.; Mattavelli, P.; Shen, Z. Analysis of D-Q Small-Signal Impedance of Grid-Tied Inverters. *IEEE Trans. Power Electron.* **2016**, *31*, 675–687. [\[CrossRef\]](#)
10. Fang, J.; Li, X.; Li, H.; Tang, Y. Stability Improvement for Three-Phase Grid-Connected Converters Through Impedance Reshaping in Quadrature-Axis. *IEEE Trans. Power Electron.* **2018**, *33*, 8365–8375. [\[CrossRef\]](#)
11. Tu, C.; Gao, J.; Xiao, F.; Guo, Q.; Jiang, F. Stability Analysis of the Grid-Connected Inverter Considering the Asymmetric Positive-Feedback Loops Introduced by the PLL in Weak Grids. *IEEE Trans. Ind. Electron.* **2022**, *69*, 5793–5802. [\[CrossRef\]](#)
12. Tonkoski, R.; Turcotte, D.; EL-Fouly, T.H.M. Impact of High PV Penetration on Voltage Profiles in Residential Neighborhoods. *IEEE Trans. Sustain. Energy* **2012**, *3*, 518–527. [\[CrossRef\]](#)
13. Eftekharijad, S.; Vittal, V.; Heydt, G.T.; Keel, B.; Loehr, J. Impact of Increased Penetration of Photovoltaic Generation on Power Systems. *IEEE Trans. Power Syst.* **2013**, *28*, 893–901. [\[CrossRef\]](#)
14. Tamimi, B.; Cañizares, C.; Bhattacharya, K. System Stability Impact of Large-Scale and Distributed Solar Photovoltaic Generation: The Case of Ontario, Canada. *IEEE Trans. Sustain. Energy* **2013**, *4*, 680–688. [\[CrossRef\]](#)
15. Pourbeik, P.; Sanchez-Gasca, J.J.; Senthil, J.; Weber, J.D.; Zadkhast, P.; Kazachkov, Y.; Tacke, S.; Wen, J.; Ellis, A. Generic Dynamic Models for Modeling Wind Power Plants and Other Renewable Technologies in Large-Scale Power System Studies. *IEEE Trans. Energy Convers.* **2017**, *32*, 1108–1116. [\[CrossRef\]](#)
16. Markovic, U.; Stanojev, O.; Aristidou, P.; Vrettos, E.; Callaway, D.; Hug, G. Understanding Small-Signal Stability of Low-Inertia Systems. *IEEE Trans. Power Syst.* **2021**, *36*, 3997–4017. [\[CrossRef\]](#)
17. Bosgra, O.H. Multivariable Feedback Control - Analysis and Design. *IEEE Control Syst. Mag.* **2007**, *27*, 80–81. [\[CrossRef\]](#)
18. Pogaku, N.; Prodanovic, M.; Green, T.C. Modeling, Analysis and Testing of Autonomous Operation of an Inverter-Based Microgrid. *IEEE Trans. Power Electron.* **2007**, *22*, 613–625. [\[CrossRef\]](#)
19. Huang, L.; Wu, C.; Zhou, D.; Blaabjerg, F. A Double-PLLs-Based Impedance Reshaping Method for Extending Stability Range of Grid-Following Inverter Under Weak Grid. *IEEE Trans. Power Electron.* **2022**, *37*, 4091–4104. [\[CrossRef\]](#)
20. Harnefors, L.; Bongiorno, M.; Lundberg, S. Input-Admittance Calculation and Shaping for Controlled Voltage-Source Converters. *IEEE Trans. Ind. Electron.* **2007**, *54*, 3323–3334. [\[CrossRef\]](#)
21. Sun, J. Impedance-Based Stability Criterion for Grid-Connected Inverters. *IEEE Trans. Power Electron.* **2011**, *26*, 3075–3078. [\[CrossRef\]](#)
22. Wang, X.F.; Song, Y.; Irving, M. *Modern Power Systems Analysis*; Springer: Berlin/Heidelberg, Germany, 2008.

23. Harnefors, L. Modeling of Three-Phase Dynamic Systems Using Complex Transfer Functions and Transfer Matrices. *IEEE Trans. Ind. Electron.* **2007**, *54*, 2239–2248. [[CrossRef](#)]
24. Jayasinghe, G.; Bahrani, B. Stability-Enhancing Measures for Weak Grids Study. Report, Monash University. 2021. Available online: https://scholar.google.com/scholar?hl=en&as_sdt=0%2C5&q=+Stability-Enhancing+Measures+for+Weak+Grids+Study&btnG= (accessed on 30 April 2024).

Disclaimer/Publisher’s Note: The statements, opinions and data contained in all publications are solely those of the individual author(s) and contributor(s) and not of MDPI and/or the editor(s). MDPI and/or the editor(s) disclaim responsibility for any injury to people or property resulting from any ideas, methods, instructions or products referred to in the content.